Journal of Cleaner Production 419 (2023) 138200

Contents lists available at ScienceDirect

Journal of Cleaner Production

journal homepage: www.elsevier.com/locate/jclepro

Solar photoelectrocatalytic oxidation of urea in water coupled to green hydrogen production

Adriana Rioja-Cabanillas [a,b,*], Stuart McMichael [a], Alvaro Tolosana-Moranchel [c], Salem Alkharabsheh [a], Nathan Skillen [d], Pilar Fernandez-Ibañez [a], John Anthony Byrne [a,**]

[a] Nanotechnology and Integrated Bioengineering Centre, School of Engineering, Ulster University, BT15 1ED, Belfast, United Kingdom
[b] Delft Intensified Materials Production, Molengraaffsingel 8, 2629 JD, Delft, Netherlands
[c] Grupo de Energia y Quimica Sostenibles, Instituto de Catalisis y Petroleoquimica, CSIC, Marie Curie 2, 28049, Madrid, Spain
[d] School of Chemistry and Chemical Engineering, Queen's University Belfast, BT9 5AG, Belfast, United Kingdom

ARTICLE INFO

Handling Editor: Panos Seferlis

Keywords:
Urea oxidation
Photoelectrochemical cell
WO_3 photoanode
Hydrogen
Wastewater treatment
Photoelectrocatalysis

ABSTRACT

In past decades, the intensification of human activities has led to an increase in pollution and energy demand. Photoelectrochemical systems have emerged as an alternative for the decentralized management of domestic wastewater with the potential of recovering energy while degrading pollutants such as urea. Tungsten oxide (WO_3) has been traditionally used for water splitting, but the use of this material for the removal of waste from water coupled to hydrogen production is not deeply known until now. This contribution shows an exhaustive and systematic investigation on WO_3 photoanodes for the photoelectrochemical oxidation of urea and the generation of hydrogen, with insights on the reaction mechanism, detailed nitrogen balance investigation of the process, and analysis of the performance compared to well-accepted materials. The WO_3 platelets were successfully synthesized in situ on fluorine doped tin oxide glass by a hydrothermal method. The performance of WO_3 was compared to titanium dioxide (TiO_2) as a benchmark. The photocurrent was enhanced for both electrodes when urea was added to the electrolyte, with WO_3 showing one order of magnitude higher photocurrent than TiO_2. The WO_3 electrode showed a peak incident photon-to-current efficiency of 43% at 360 nm and a much greater rate constant for urea oxidation (1.47×10^{-2} min^{-1}), compared to the TiO_2 photoanode (16% at 340 nm and 1.1×10^{-3} min^{-1}). The influence of different reactor configurations was also evaluated testing one- and two-compartment back-face irradiated photoelectrochemical cells. Hydrogen was generated with a Faradaic efficiency of 87.3% and a solar-to-hydrogen conversion efficiency of 1.1%. These findings aim to contribute to the development of technologies based on the photoelectrochemical production of hydrogen coupled with the oxidation of pollutants in wastewater.

1. Introduction

In the last decades, the intensification of anthropogenic activities and the rapid growth of the global population have resulted in alarming increased levels of environmental pollution and energy demand. In 2021, the worldwide demand for primary energy experienced the largest increase in history, with fossil fuels accounting for 82% of primary energy used (BP Statistical Review of World Energy, 2021). Besides carbon emissions derived by the combustion of fossil fuels, human activities are responsible for the pollution of water bodies. In this regard, nutrient pollution is one of the most widespread types of water pollution worldwide, causing adverse environmental effects such as eutrophication, harmful algal blooms, and in extreme cases the creation of dead zones. Excess of nitrogen compounds in water bodies is one of the major contributors of nutrient pollution. Urine contributes to 80% of all the nitrogen waste found in domestic wastewater, with urea ($(NH_2)_2CO$) as a major constituent (Egle et al., 2015).

Coupling the oxidation of organic and inorganic compounds to the

* Corresponding author. Nanotechnology and Integrated Bioengineering Centre, School of Engineering, Ulster University, BT15 1ED, Belfast, United Kingdom.
** Corresponding author.
E-mail addresses: Rioja_Cabanillas-A@ulser.ac.uk (A. Rioja-Cabanillas), s.mcmichael@ulster.ac.uk (S. McMichael), alvaro.tolosana@csic.es (A. Tolosana-Moranchel), alkharabsheh-s@ulster.ac.uk (S. Alkharabsheh), n.skillen@qub.ac.uk (N. Skillen), p.fernandez@ulster.ac.uk (P. Fernandez-Ibañez), j.byrne@ulster.ac.uk (J.A. Byrne).

https://doi.org/10.1016/j.jclepro.2023.138200
Received 5 March 2023; Received in revised form 30 June 2023; Accepted 20 July 2023
Available online 20 July 2023

production of hydrogen is an interesting approach to recovering energy from, and the treatment of, wastewater. Among different options for energy recovery, the production of hydrogen is an appealing option due to its high energy density and use as clean fuel. When produced in a sustainable way, hydrogen is considered a key clean energy carrier which can support a decarbonized society fueled by renewable energy. Currently however, a 95% of hydrogen is still produced by fossil fuel-based processes such as methane reforming and gasification of oil or coal (IRENA, 2021). The average urine excretion of an adult human is estimated to be app approximately 1.5 L/day, with an average urea concentration in urine of 22 g/L (Lens et al., 2005; Rollinson et al., 2011). Considering that urea contains 6.7 wt% hydrogen, the potential recovery is estimated to 400 g of H_2 per person annually. This would result in an annual recovery of 48 MJ per person.

Photo-electrochemical cells (PEC) can be used to recover energy from wastewater. Photoelectrocatalysis uses a solar driven semiconductor photoanode which is able to oxidize organic and inorganic waste compounds. The photogenerated electrons are passed via an external circuit to the counter electrode for the reduction of H^+ to H_2. The counter electrode may be either a metallic or carbon conducting electrode, or a semiconductor photocathode (with or without a photoanode). If operating without an external electrical bias, the PEC behaves as a photogalvanic cell, i.e. generating electricity from the oxidation of compounds in the wastewater (Fernandez-Ibanez et al., 2021; Rioja--Cabanillas et al., 2020).

The thermodynamic potential for water splitting is 1.23 V but the potential for reforming some organic and inorganic compounds to yield hydrogen can be much lower, e.g. the oxidation of urea is more favorable with a standard reduction potential of - 0.46 V (Boggs et al., 2009), resulting in an overall cell potential for the production of H_2 from urea of 0.37 V.

Among the different semiconductors, TiO_2 has been widely used due to its high photo-activity, low cost and good chemical and thermal stability. While TiO_2 has been studied for a range of diverse applications including hydrogen production (Reddy et al., 2020) and degradation of organic pollutants (Pelaez et al., 2012), there are fewer examples for the photocatalytic oxidation of urea (Calza et al., 2005; Park et al., 2019; Pelizzetti et al., 2004). WO_3 has been studied as an alternative to TiO_2, due to its narrower band gap, which extends into the visible region of the solar spectrum. It also presents good stability and charge carrier mobility, and resistance to photo-corrosion (Liu et al., 2012). A variety of methods for the fabrication of WO_3 photoanodes have been reported including anodizing of W foils, sol-gel, hydrothermal and pulsed laser deposition (Kalanur et al., 2018). WO_3 photoanodes have been widely studied for water splitting (Kalanur et al., 2018), however to date, only some works have investigated urea oxidation (Shen et al., 2019a, 2019b, 2020).

While most photoelectrochemical works have focused on either hydrogen production from water splitting or on the degradation of pollutants, only limited studies have investigated the production of energy coupled with wastewater treatment. In 2006, Kaneko et al. demonstrated the possibility of generating electricity by decomposing different pollutants (including urea) using a TiO_2 photoanode and a O_2-reducing cathode. Since then very few studies have highlighted the recovery of energy in the form of electricity (Dector et al., 2021) or H_2 from urea using TiO_2 based photoanodes (Pop et al., 2015; Wang et al., 2012). The low photo-current densities reached using TiO_2 under simulated solar irradiation, however, limit the applicability of this approach.

The aim of this article is to showcase the simultaneous photoelectrochemical oxidation of urea and the production of hydrogen using a WO_3 photoanode with a platinized titanium cathode in a two compartment photoelectrochemical cell. The photoelectrochemical behavior of WO_3 was compared to TiO_2. Urea oxidation kinetics and product distribution were investigated using two custom-made photoelectrochemical cells. The findings presented in this study demonstrate the proof of concept of oxidizing common pollutants present wastewater as urea, coupled to the simultaneous generation of hydrogen in a photoelectrochemical cell.

2. Materials and methods

All chemicals used in this study were of analytical grade; details are available in Supplementary data Section S1.

2.1. Photoanode fabrication

The TiO_2 photoanode was fabricated by the immobilization of commercial P25 on a fluorine doped tin oxide (FTO) coated glass using spray coating, achieving a desired loading of 1 mg cm^{-2} (the procedure is described in Section S2.1). This value was chosen based on previous studies that described the optimal loading for the degradation of formic acid and atrazine (McMurray et al., 2004, 2006).

The WO_3 photoanode was synthesized directly on the FTO glass using a hydrothermal process described in Section S2.2, (Yang et al., 2012). Subsequentially, the FTO coated glasses were extracted, rinsed with distilled water, and dried in ambient air before annealing. Both the TiO_2 and WO_3 coated FTO coupons were annealed in a Lenton furnace at 450 °C in air for 1 h using a ramp rate of 2 °C min^{-1}.

The electrical contacts for the 1.5 cm × 2 cm electrodes were made by attaching a Cu wire to the FTO area not coated with the semiconductor, using conductive silver epoxy. The contact and any uncoated area were then insulated using SU8 photoresist leaving an active photoanode area of 1.5 × 1 cm^2. The SU8 coated samples were first dried in the oven, then cured by exposing them to UVB irradiation followed by a hard bake at 160 °C for 30 min.

2.2. Material characterization

The surface morphology of the photoanodes was characterized using scanning electron microscope (Hitachi SU500 FE-SEM) with an accelerating voltage of 10 kV and a high vacuum pressure of 10^{-8} bar. The size of the nanoparticles was determined using the software ImageJ averaging more than 50 measurements.

The elemental composition of the electrodes was determined by X-ray photoelectron spectroscopy (XPS) (Kratos Axis Ultra). The wide energy survey scans (WESS) were measured for all samples in the binding energy range of 0–1250 eV, with a pass energy of 160 eV. High resolution (HR) scans of each target element (C, Ti, W and O) were recorded with a pass energy of 14.2 eV.

The crystalline phase of the WO_3 photoanode was characterized using X-ray diffraction (XRD) (Malvern Panalytical) with Cu Kα (λ = 1.560 Å) radiation at a scanning angle between 20° and 70°.

The UV–vis diffuse reflectance spectra were measured with a LAMBDA 365 UV/Vis spectrometer (PerkinElmer) equipped with an integrating sphere and the optical band gap was estimated using the Kubelka-Munk method.

2.3. Electrochemical characterization

The photoelectrochemical characterization was performed using an electrochemical workstation (AUTOLAB PGSTAT 30) and a 450 W Xe lamp (Horiba Jobin Yvon FL-1039/40, Fig. S1) equipped with a monochromator (Horiba Jobin Yvon microHR), a chopper (Uniblitz) for interrupted irradiation and an infra-red (IR) filter. The irradiance (I) from the Xe lamp was measured using a radiometer (Ocean Optics) and the spectrum is reported in Fig. S1. In each photoelectrochemical measurement, the photoanode was used as the working electrode with a Pt mesh as counter and a saturated calomel electrode (SCE) as reference. The experiments were performed in a 30 mL one compartment cylindrical cell made of quartz glass, using 0.05 M $KClO_4$ as electrolyte.

The linear sweep voltammetry (LSV) and spectral photocurrent

measurements were performed to evaluate the performance of the photoanodes under different potential and spectral conditions. In the LSV, a scan rate of 5 mV s^{-1} was used. The spectral photocurrent response measurements were performed from a wavelength ranging from 280 nm to 500 nm in steps of 10 nm with chopped irradiation intervals of 20 s and a fixed potential of 1 V vs SCE. The incident photon to current efficiency (IPCE) was determined using equation S1 described in Section S4:Efficiency equations.

2.4. Urea degradation and hydrogen production experiments

One and two compartment PECs were designed and fabricated using a high resolution stereolithography 3D printer (Formlabs Form 2) and a chemical resistant clear resin (Formlabs RS-F2-GPCL-04). After the parts were printed, they were thoroughly washed with isopropanol and cured at 60 °C for 40 min, and then cleaned again with MilliQ water. A schematic representation of both cells is shown in Fig. 1. The PECs were designed for back-face irradiation of the photoanode, with an irradiated area of 19.6 cm^2. The FTO glass with the deposited semiconductor was placed between two O-rings, which seal the system to avoid electrolyte leaking. The electrical contact of the photoanode was made by contacting the FTO glass with a copper plate. A commercial platinized (2.5 ± 0.3 μm) titanium mesh was used as cathode. The cells were equipped with septum ports to facilitate the extraction of liquid samples using syringes. The one-compartment cell, shown in Fig. 1a, had a total volume of 33 mL and an electrode separation of 10 mm. In the two-compartment PEC (Fig. 1b), a Nafion membrane, placed between two

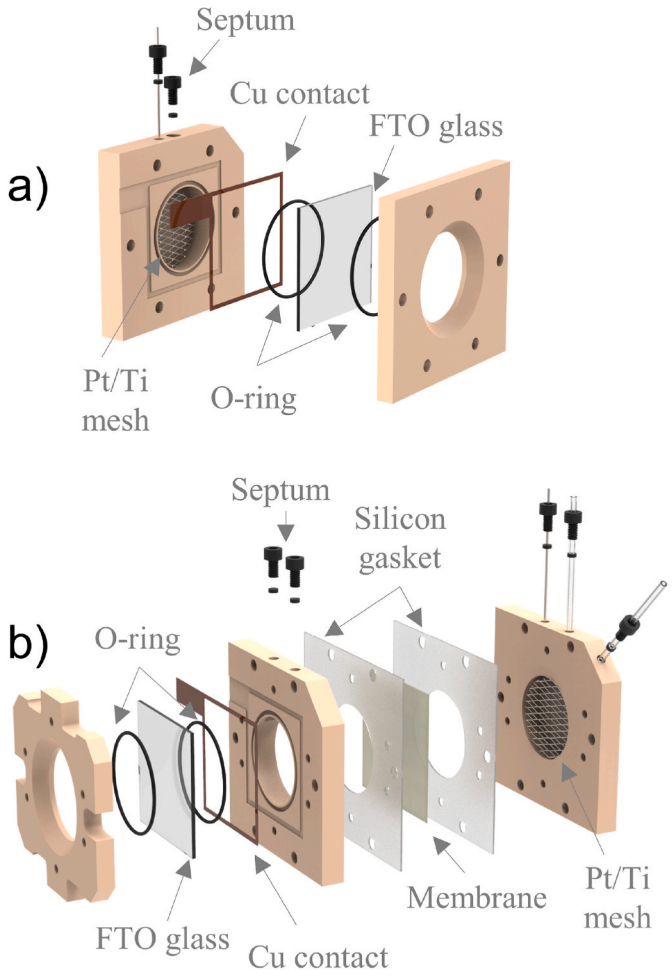

Fig. 1. 3D exploded view of the (a) one-compartment and (b) two-compartment PECs.

silicon gaskets, was used to separate the anolyte from the catholyte. Each compartment had a volume of 33 mL and the distance between electrodes was 15 mm. The electrolyte consisted of 0.05 M $KClO_4$ and known concentrations of either urea, nitrate or ammonium with an initial pH of 6.2.

The irradiation source was a 1000 W Xe lamp (Quantum Design, Fig. S1). A power supply (PHL120 DC Aim-TTi) was used to provide the external electrical bias and multimeters were used to record the potential and current (1351 Data precision).

The quantification of the N-species in aqueous phase including, NH_4^+, NO_3^- and NO_2^- was performed following the spectrophotometric methods described in the ISO 15923–1(Water quality — Determination of selected parameters by discrete analysis systems BS ISO 15923-1:2013, 2013) using a UV/Vis spectrometer (PerkinElmer). The concentration of urea was determined by a colorimetric method previously reported by Jung et al. (1975) and Zawada et al. (2009) (See Section S5 for more detail). The detection of hydrogen gas was performed using a gas chromatograph (GC - Agilent Technologies 7280 A) equipped with a thermal conductivity detector (TCD). Separation of the gas sample was achieved using a molecular sieve packed stainless steel column (MoleSieve 5A, Mesh 80/100, 6 ft length and 2 mm ID, RESTEK). The injector was driven at a pressure of 26.1 psi, a temperature of 150 °C and a flow rate of 22.9 mL min^{-1}. The flow rate employed in the column was 20 mL min^{-1} and the oven temperature was 50 °C, while the detector was kept at 200 °C with a flow rate of 5 mL min^{-1}. The peak position was determined by the injection of pure H_2, while the quantification was obtained using a calibration curve with known concentrations. Gas samples with a volume of 0.1 mL were injected into the GC using a gas tight syringe. The quantification of the total volume of gas produced during the urea degradation experiments was carried out by water displacement through a gas tight connection of the catholyte headspace to an inverted graduated cylinder. The gas generated in the cathode compartment was collected in a Tedlar sampling bag (Restek). Before performing experiments, the catholyte compartment was purged for 20 min with N_2 gas to remove the oxygen from the electrolyte.

3. Results and discussion

This section presents and discusses in detail the results obtained in this study including material characterization, photoelectrochemical characterization, and the oxidation of urea coupled to the production of hydrogen.

3.1. Material characterization

SEM was performed to analyze the surface morphology of the TiO_2 and WO_3 photoanodes (Fig. 2a and b). The image at low and high magnification of the TiO_2 photoanode (Fig. 2a) shows agglomerates of small spherical P25 nanoparticles covering the FTO surface. The nanoparticles preserved their average pre-immobilization size of 27 nm. The SEM image of the WO_3 photoanode, at low and high magnification reveals the surface of the FTO glass to be uniformly covered with a plate-like structures (Fig. 2b). The average length was 1000 nm and average thickness was 200 nm.

The chemical composition of both photoanodes was analyzed by XPS. The survey spectra (Fig. S3) showed the presence of Ti, O and C on the TiO_2 electrode and W, O and C on the WO_3 electrode, with no significant contamination. The Ti 2p spectra corresponding to the TiO_2 photoanode shows the clearly defined Ti(IV) 2 $p_{3/2}$ peak located at a binding energy (BE) of 458.6 eV, and the Ti $2p_{1/2}$ at 464.3 eV, separated by 5.7 eV (Fig. 2c) (Alov, 2005). The observed Ti^{4+} confirms, with the corresponding O 1s component, the presence of TiO_2. Additionally, the doublet $2p_{3/2}$ and $2p_{1/2}$ located at BE of 457.2 and 461.6 respectively, reveals a minor contribution from the lower oxidation state (+3) due to oxygen vacancies (Bharti et al., 2016). The W 4f spectra of the WO_3 photoanode shows two main peaks separated by 2.2 eV and attributed to

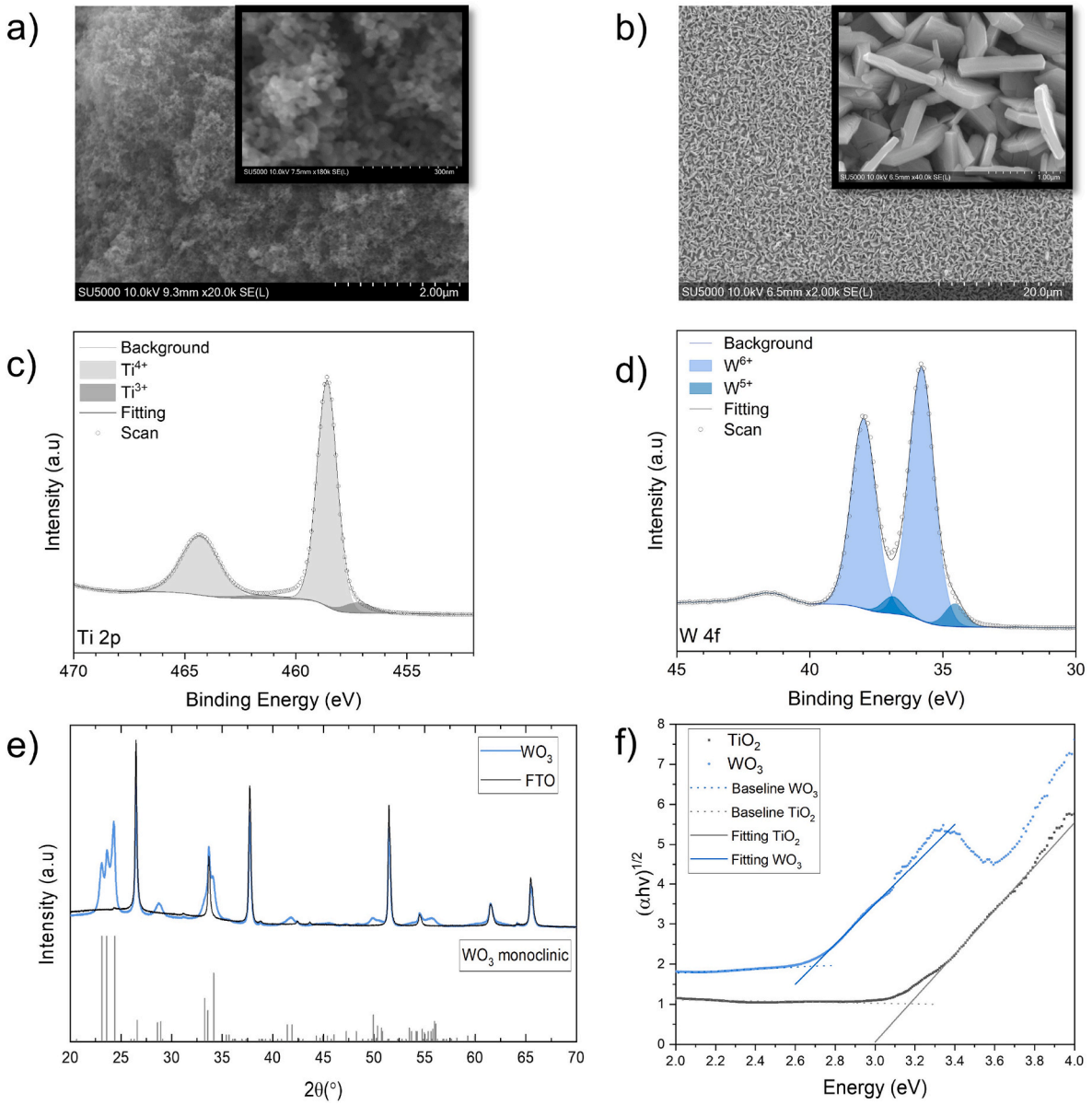

Fig. 2. Top view SEM image of a)TiO_2 and b)WO_3 photoanodes. XPS spetra corresponding to c)Ti 2p for TiO_2. photoanode and d) W4f for WO_3 photoanode. e) XRD patterns of FTO and WO_3 and f) Tauc plots for TiO_2 and WO_3.

the doublet W $4f_{7/2}$ and $4f_{5/2}$ (Fig. 2d). These contributions positioned at BE of 35.8 eV and 38 eV, are characteristic of the electronic state of W^{6+} in WO_3. Moreover, the presence of two minor contributions at slightly lower BE of 34.6 eV and 36.9 eV can be attributed to the doublet $4f_{7/2}$ and $4f_{5/2}$ from the electronic structure of W^{5+}, originated by the presence of oxygen vacancies (Fig. S4) (Corby et al., 2020; Greiner et al., 2012).

The XRD patterns of the WO_3 grown film after calcination are shown in Fig. 2e, with the FTO glass patterns also shown for easier identification of WO_3 peaks. All the diffraction peaks of the WO_3 plates agree well with the monoclinic crystal phase of WO_3, (PDF no.43-1035) with lattice constants of a = 7.297, b = 7.539 and c = 7.688 Å.

The optical band gap energies were estimated from the diffuse reflectance measurements using the Tauc plots shown in Fig. 2f. An optical band gap of 3.2 eV was obtained for the electrode formed by P25 deposited on FTO, which agrees with previous literature values of 3.2 eV for anatase and 3.0 eV for rutile, with P25 being a mixture of 80% anatase and 20% rutile (Pelaez et al., 2012). The optical band gap for the WO_3 plates grown on FTO was 2.7 eV which, correlates to previously reported values for WO_3 nanostructures of 2.5–2.8 eV (Dutta et al., 2021; Pelaez et al., 2012; Zheng et al., 2019).

3.2. Photoelectrochemical characterization

The photoelectrochemical characteristics of the fabricated electrodes were evaluated by LSV under chopped irradiation, spectral photocurrent response and IPCE. The current response of both anodes was measured in a potential ranging from 0.0 to +1.5 V vs SCE (Fig. 3a). The TiO_2 photoanode showed a photocurrent density of 40 μA cm^{-2}, which is stable in the studied potential range, while the WO_3 photoanode showed an increasing photocurrent density, reaching a saturation current density of 402 μA cm^{-2} at +1.5 V. The maximum current value obtained with WO_3 is 10 times higher than the one measured with TiO_2. Chronoamperometry measurements of both electrodes are shown in Section S8. Different current densities have been reported for different WO_3 structures, varying from 150 μA cm^{-2} to 2500 μA cm^{-2} (Li et al., 2014, 2016; Liu et al., 2019, 2020; Tolosana-Moranchel et al., 2022; Zheng et al., 2019), while reported values for P25 photoanodes vary from 1 μA

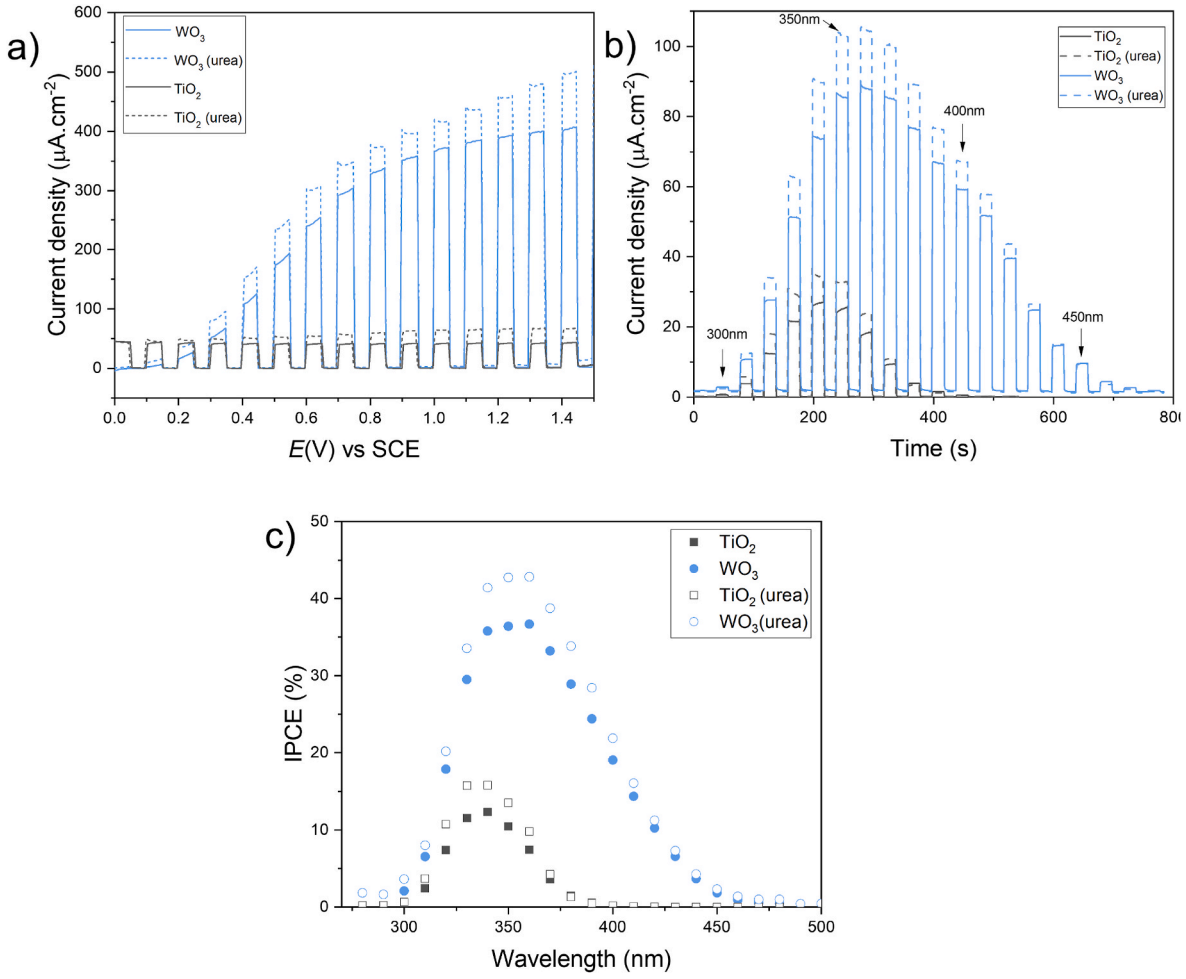

Fig. 3. a) Linear sweep voltammograms under chopped irradiation, working window: 0 to +1.5 V, scan rate = 5 mV s^{-1}, b) spectral current response at fixed potential (1.0 V vs SCE) with monochromatic irradiation (280 nm–500 nm) c) Incident photon-to-current efficiency (IPCE). I_0 (280–500 nm) = 178 W m^{-2}. Electrolyte = 50 mM $KClO_4$ with or without 6.6 mM urea.

cm^{-2} to 1000 μA cm^{-2} (Haisch et al., 2017; Kim et al., 2013; Pop et al., 2015; Ranganathan et al., 2016; Yang et al., 2019; Yu et al., 2014). A direct comparison of these values is unfortunately not possible due to the different experimental conditions, such as the radiation intensity, spectral output of the irradiation source, the electrolyte and the photoelectrochemical cell design. To study the electrode behavior at negative potentials and measure the onset photocurrent potential, a LSV was performed from −1.0 to +1.5 V vs SCE (Fig. S5), for TiO_2 photoanode the onset potential for anodic current was −0.6 V vs SCE, while for WO_3 the onset potential for anodic current was +0.15 V vs SCE. The critical band bending ($\varnothing_s$) is the difference between the onset potential (close to flat band E_{fb}) and the potential required to obtain the maximum or saturated photocurrent (where all charge carriers are separated). For TiO_2 $\varnothing_s$ is around 0.5 V (Fig. S5) while for the WO_3 the photocurrent continues to increase asymptotically up to 1.5 V ($\varnothing_s \sim 1.35$ V), but a much larger photocurrent is observed. Multiple factors can account for the better performance of the WO_3 photoanode at more positive potentials, compared to the TiO_2. The plate-like structure of WO_3 presents a direct pathway for the photogenerated charges to the current collector (Zeng et al., 2017; Zheng et al., 2019). On the other hand, the TiO_2 photoanode has a porous structure formed from P25 independent particles. This structure limits photogenerated charge transfer efficiency through the particles and to the collector electrode (FTO glass), increasing the interparticle charge recombination (Wang et al., 2020). In addition to morphological differences, when comparing the spectral photocurrent response (Fig. 3b), WO_3 showed a superior photocurrent density than TiO_2, at any point in the spectrum. Furthermore, WO_3 exhibited visible light activity up to 470 nm while TiO_2 gave photocurrent up to 390 nm. These wavelengths correspond to an effective bandgap of 2.63 eV for WO_3 and 3.18 eV for TiO_2, which are consistent with the optical band gap determined from the Tauc plots, and correlate to values previously reported (Pelaez et al., 2012; Reddy et al., 2020). The IPCE efficiency of WO_3 peaks with 37% at a wavelength of 360 nm, while TiO_2 peaks with 12% at 340 nm (Fig. 3d). The IPCE values obtained for WO_3 are in line with several studies using WO_3 nanoparticulate photoanodes (Li et al., 2016; Liu et al., 2019, 2020; Zeng et al., 2017). The IPCE values reported in previous studies for P25 photoanodes vary widely (10–25%) (Haisch et al., 2017; Ranganathan et al., 2016; Tolosana-Moranchel et al., 2022; Yang et al., 2019), due to the different experimental conditions, including the electrode thickness, immobilization process, electrolyte and testing conditions; nevertheless, the value reported in this work is within the range reported in comparable studies.

An increase in the photocurrent density due to the addition of urea was observed for both electrodes, which may be attributed to the oxidation of urea via direct hole transfer or via hydroxyl radical mediated hole transfer (Fig. 3a) both resulting in hole capture and reduced rates of charge carrier recombination. The photocurrent magnitude depends on the concentration of urea in solution. An increase in photocurrent due to the presence of urea has been previously reported in two studies using TiO_2 photoanodes. Kim et al. (2012) reported a 3-fold increase in photocurrent with a concentration of 0.33 M urea and Pop

et al. (2015) reported an enhancement varying from 15% to 35% with urea concentrations ranging from 0.1 to 1 M. In this work, with urea concentration of 6.6 mM, a 45% increase in photocurrent for the TiO_2 photoanode is reported. Moreover, this study also tested a WO_3 photoanode in the presence of urea, observing a 25% increase in photocurrent. The spectral photocurrent response was also measured in presence of urea (Fig. 3c). For WO_3 the peak efficiency increased to 43% at a wavelength of 360 nm, while TiO_2 improved to 16% at 340 nm.

Overall, the photoelectrochemical results showed an improved performance for WO_3, when compared to TiO_2, which is attributed to an increased light absorption range in the UV–vis due to the lower bandgap energy and an enhanced pathway for the charge carrier migration.

3.3. One-compartment cell: urea degradation experiments

The performance of TiO_2 and WO_3 photoanodes in the custom-made PEC (Fig. 1a) was investigated by varying the applied cell potential between the photoanode and the platinized titanium mesh cathode (Fig. 4a). Simultaneously, the photoanode potential was measured using a reference electrode as shown in Fig. 4b. The current generated under irradiation by the TiO_2 photoanode increases slightly with increasing applied cell potential (Fig. 4a), for the dark current, breakdown was observed at a potential of 1.2 V. The chosen operating cell potential for TiO_2 was 1.2 V with a photoanode potential of +1.14 V vs SCE, as this was the point of current saturation.

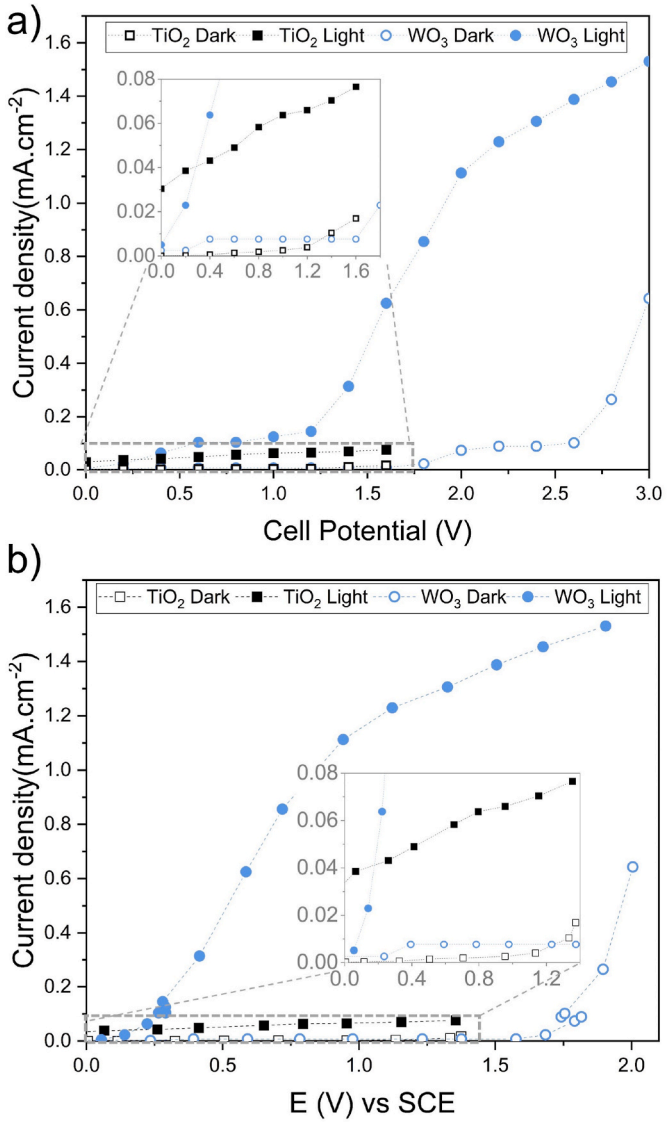

Fig. 4. a) Measured current for TiO_2 and WO_3 at different cell potentials b) Current for anode potential vs SCE measured while varying cell potential for TiO_2 and WO_3. All measurement were carried out in the one-compartment photoelectrochemical cell. I_0 (280–500 nm) = 173 W m^{-2}. Anode geometrical area = 19.6 cm^{-2}. Electrolyte = 50 mM $KClO_4$ and 0.83 mM Urea.

The saturation current for the WO_3 photoanode was substantially higher than for TiO_2, however a greater applied potential is also required to achieve this current (Fig. 4a). The breakdown current for WO_3 photoanode is observed at a cell potential of 2.5 V, corresponding to a photoanode potential of +1.55 V vs SCE. Under irradiation, for increasing cell potential between 0.5 and 1.25 V (Fig. 4a), the anode potential remains fairly constant (+0.31 to +0.32 V vs SCE) (Fig. 4b). Similarly, in the dark for cell potential between 2.0 and 2.5 V (Fig. 4a) the anode potential remains between +1.79 and +1.81 V vs SCE (Fig. 4b). This trend is attributed to the contribution of the cathode and the ohmic drop to the cell potential. The cell potential of 2.4 V was chosen within the saturation region, corresponding to an anode potential of +1.37 V vs SCE.

The current densities recorded using the one-compartment custom-made PEC (Fig. 4b) were higher compared to the quartz cell (Fig. 3a), in the whole range of the applied potentials. This enhancement is caused by the design of the photoelectrochemical cell (Fig. 1). This includes lower reflective losses due to planar FTO compared to the cylindrical water-jacketed quartz cell (further information in supplementary data Section S9).

The activity of the TiO_2 and WO_3 photoanodes for urea removal was studied over a period of 2.4 h (Fig. 5a). The TiO_2 photoanode achieved only 13% of urea oxidation while the WO_3 photoanode showed 90% of urea oxidation at the same time. The experimental data are fitted to a pseudo-first-order kinetic model (Fig. 5b), where C_0 is the initial concentration and C_t the concentration measured at time t. The obtained rate constant (k_1) for WO_3 is 1.47×10^{-2} min^{-1}, is 15 times higher than the one obtained for TiO_2 (1.1×10^{-3} min^{-1}).

To further investigate the difference in performance between WO_3 and TiO_2, additional experiments with the PEC in open circuit configuration (photocatalysis) were performed. For WO_3, the results showed urea removal values less than 5% after 2.4 h, and a rate constant of 3×10^{-4} min^{-1} (Fig. 5c). The negligible urea oxidation is due to the positive conduction band edge potential of WO_3 which is not negative enough to reduce molecular oxygen to superoxide, leading to a build-up of photogenerated electrons and recombination of charge carriers dominates. On the contrary, when a bias is applied, electrons are driven to the cathode, and the recombination is reduced, leading to improved performance. In the case of TiO_2, (Fig. S9), the decrease in the urea concentration obtained at open circuit was 7% with a rate constant of 5×10^{-4} min^{-1}, showing just a small difference between the open circuit and applied bias. The favorable position of P25–TiO_2 conduction band edge enables the use of the photogenerated electrons to reduce molecular oxygen, with the holes being used for urea oxidation (Pelaez et al., 2012). However, when a bias is applied, the morphology of P25–TiO_2 hinders electron transfer, and favors surface recombination. This recombination hampers TiO_2 photoanode performance in comparison to WO_3, as discussed in section 3.2 Photoelectrochemical characterization.

The reusability of the WO_3 photoanode for urea oxidation is studied over 5 consecutive cycles each 2.4 h, as shown in Fig. 5d. The photoanode reveals similar activity with urea concentration decreasing by between 90% and 82% at the end of each cycle, which results in rate constants ranging from 1.47×10^{-2} min^{-1} to 1.2×10^{-2} min^{-1}. Only a slight decrease can be observed in the last cycle after 12 h.

The analysis of the time distribution of the nitrogen ionic species present in the solution from the oxidation of urea in the custom-made one-compartment PEC reveals that the prevalent species are NH_4^+ and NO_3^-, reaching up to 0.86 mM and 0.70 mM, respectively at the end of the experiment, and nearly non-detectable concentrations of NO_2^- (8×10^{-3} mM) (Fig. 6). The totality of the quantified N-ionic species balances

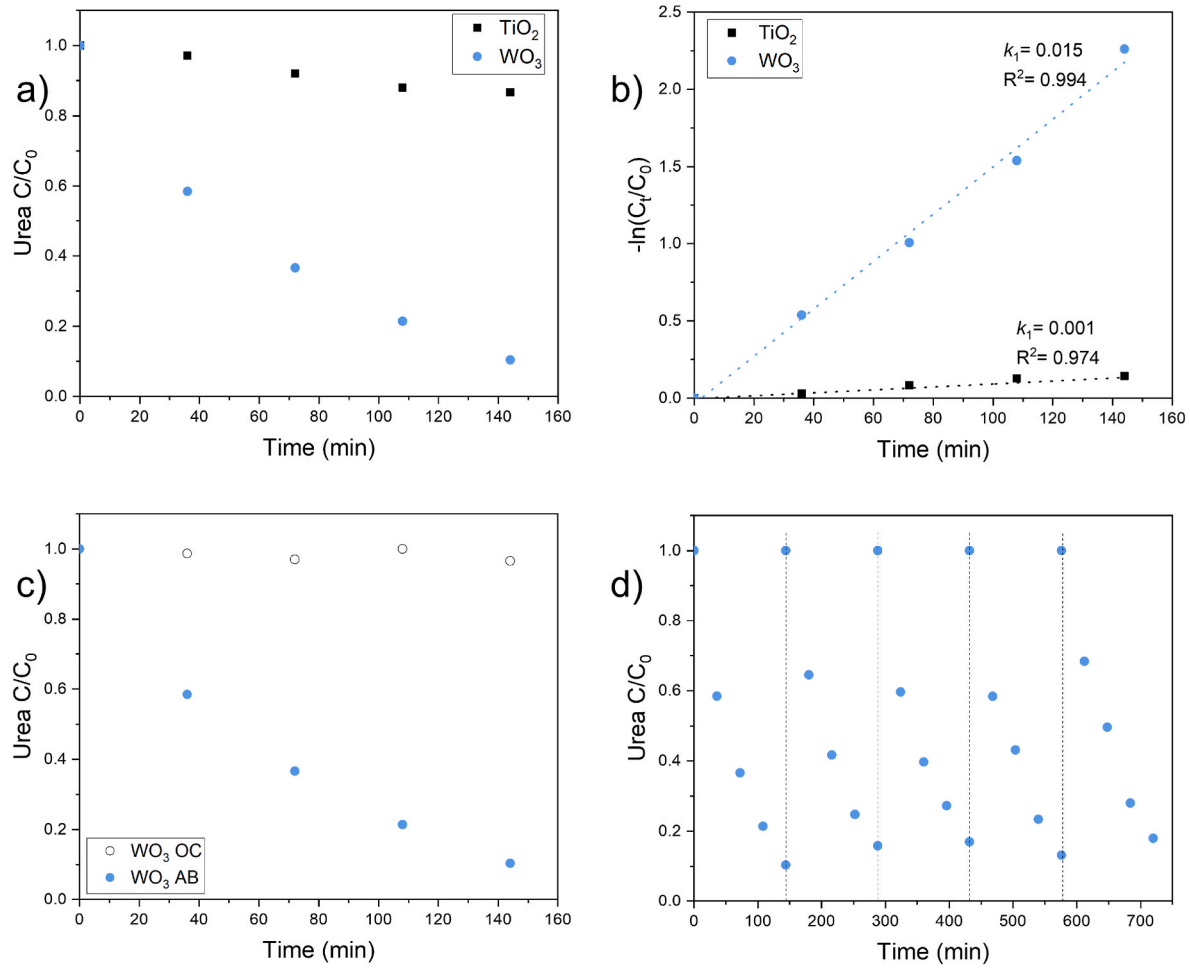

Fig. 5. a) Normalized urea concentration vs time for TiO_2 and WO_3 electrodes and b) negative natural log of normalized concentration vs time for TiO_2 and WO_3, c) Normalized urea concentration vs time for WO_3 electrodes at open circuit (OC) and with applied bias (AB), d) Normalized urea concentration vs time for 5 consecutive experiments with the WO_3 electrode. $[Urea]_0$ = 0.83 mM. Electrolyte = 0.05M $KClO_4$. I_0 (280–500 nm) = 173 W m^{-2}.

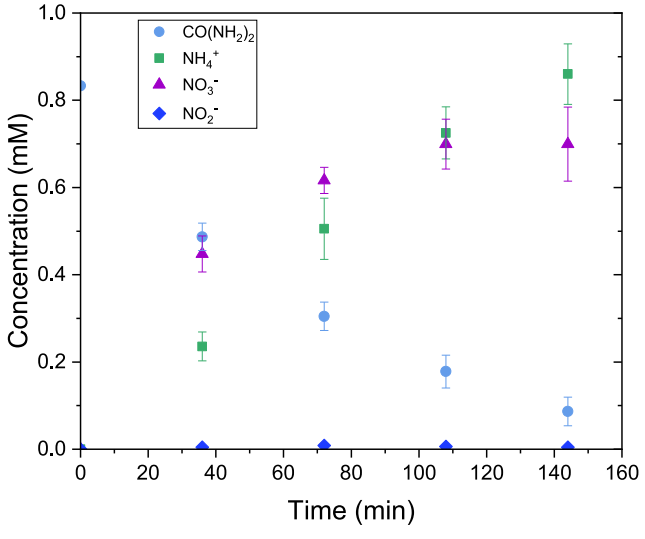

Fig. 6. Time evolution of urea conversion to NH_4^+, NO_3^- and NO_2^- using WO_3 photoanode. One-compartment cell. $[Urea]_0$ = 0.83 mM. Electrolyte = 0.05M $KClO_4$. I_0 (280–500 nm) = 173 W m^{-2}.

the nitrogen content in this process, suggesting that no N_2 gas or other aqueous N-species were originated from the oxidation of urea under these conditions (Equation S4).

Hydroxyl radicals (·OH) have been reported to have a major role in the oxidation of urea to form NO_3^- and NH_4^+ (Calza et al., 2005; Park et al., 2019; Pelizzetti et al., 2004). Previous studies described a detailed mechanism for the photocatalytic oxidation of urea using TiO_2 (Calza et al., 2005; Park et al., 2019; Pelizzetti et al., 2004). Pelizzetti et al. (2004) proposed a mechanism for urea degradation using TiO_2, where, one of the amino groups of urea initially converts into a nitroso group and later to a nitro group by ·OH. Subsequentially, the nitroformamide is hydrolyzed, releasing NO_2^- ions, which are rapidly transformed into NO_3^- by ·OH (Zafra et al., 1991). The remaining carbamic acid, which occurs as a zwitterion can undergo two different oxidation pathways. One of the possible pathways is the oxidation to CO_2 and NH_2OH by ·OH radicals, NH_2OH undergoes further ·OH oxidation to NO_2^- and NO_3^-. The other possible pathway is the decomposition of carbamic acid to form HCO_3^- and NH_3 by simultaneous ·OH and e^- attacks. The molar ratio of NO_3^- to NH_4^+ is indicative of which reactions are favored. NO_3^-/NH_4^+ ratios of 2 (Calza et al., 2005) and 1.9 (Park et al., 2019) have been reported for photocatalytic degradation of urea using TiO_2. Alternatively, Kim et al. (2012) reported no NO_3^- production in anoxic conditions, suggesting that the presence of O_2 is essential for the generation of NO_3^- from the photocatalytic degradation of urea in TiO_2.

In this study, with the WO_3 photoanode, the production of NO_2^- in time peaks at 8×10^{-3} mM after 72 min and then decreases, indicating

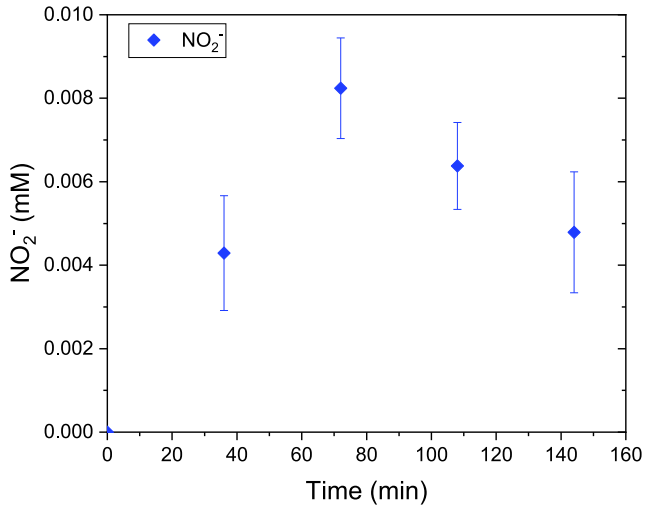

Fig. 7. Evolution of NO_2^- concentration in time during oxidation of urea with WO_3. One-compartment cell. WO_3 photoanode. I_0 (280–500 nm) = 173 W m^{-2}. Electrolyte = 0.05M $KClO_4$. $[Urea]_0$ = 0.83 mM.

that NO_2^- is a reaction intermediate (Fig. 7), which is consistent with the proposed rapid oxidation of NO_2^- to NO_3^- (Zafra et al., 1991). However, a higher molar concentration of NH_4^+ than NO_3^- was obtained with a ratio of 0.81 $[NO_3^-]/[NH_4^+]$, which deviates from the previously obtained results in photocatalytic tests using TiO_2 (Calza et al., 2005; Park et al., 2019). This suggests that even though the urea oxidation via ·OH radicals in solution could follow the pathway proposed by Pelizzetti et al. (2004), there might be another mechanisms contributing to preferential decomposition to NH_4^+. The production of ·OH by the WO_3 was demonstrated in Section S11.

To gain knowledge depth on the mechanism and potential side reactions, the reduction of NO_3^- to NH_4^+, by either the cathode or electrons from the photoanode conduction band, was investigated by performing experiments starting with a 0.55 mM NO_3^- solution. The results show that 25% of the NO_3^- was converted to NH_4^+ (Fig. 8), confirming the viability of this reduction reaction in the final product distribution.

Similarly, to obtain more insight into the possible oxidation of NH_4^+ to NO_3^- and its role in the main mechanism, experiments starting with a

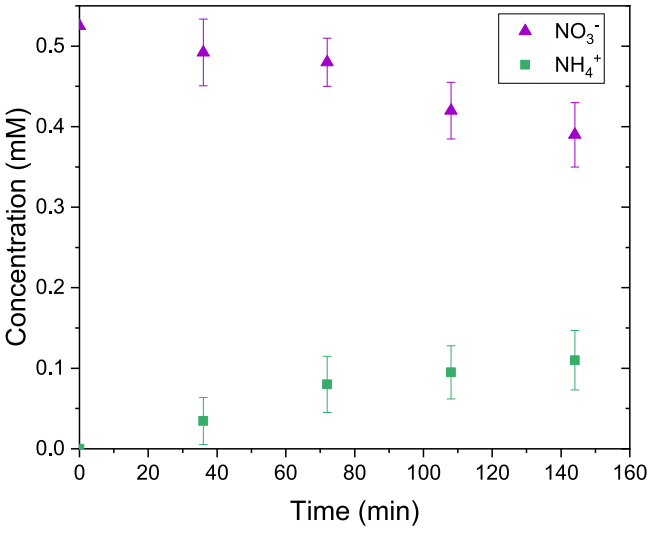

Fig. 8. Evolution of NO_3^- in time and conversion to NH_4+($[NO_3^-]_0$ = 0.55 mM). One-compartment cell. WO_3 photoanode. I_0 (280–500 nm) = 173 W m^{-2}. Electrolyte = 0.05M $KClO_4$.

0.58 mM NH_4^+ solution were performed. The results proved that NH_4^+ was not oxidized under these experimental conditions. Several studies have reported the oxidation to occur only when the un-ionized form ammonia (NH_3) is predominant for which the pH needs to be higher than 9.25 (pKa) (Michels et al., 2010; Nemoto et al., 2007; Zhu et al., 2005). In the pH used in this study (initial pH of 6.2), the protonated form ammonium (NH_4^+) will predominate.

The ionic N-species present due to urea oxidation using TiO_2 as photoanode was also studied and shown in Fig. S10, similarly to WO_3 the majority of the products are NH_4^+ and NO_3^- with low values for NO_2^- of 5×10^{-3} mM, but in this case a slightly higher molar concentration of NO_3^- was obtained over NH_4^+ with a ratio of 1.14.

3.4. Two-compartment cell: urea degradation coupled to hydrogen production

In order to couple the production of hydrogen with the degradation of urea a two-compartment gas tight PEC was designed, with the compartments separated by a proton exchange membrane (Fig. 1b). This configuration was chosen to separate the H_2 gas evolving at the cathode from the possible gases produced at the photoanode, as well as to eliminate the potential reduction of urea intermediates in the cathode. The two-compartment cell was tested using a WO_3 photoanode as it was the best performing photoelectrode in the initial experiments.

An operational cell potential of 2.4 V, was chosen to perform the experiments in the two-compartment cell since no considerable increase of photocurrent was observed above this potential (Fig. 9a). The cell potential of 2.4 V corresponds to a potential at the photoanode of +1.15 V vs SCE (Fig. 9b). The current generated from WO_3 photoanode under irradiation and in the dark were plotted against potential of cathode vs SCE (Fig. 9c). For the chosen working applied cell potential of 2.4 V, the potential measured between cathode and reference was −1 V vs SCE.

In the two-compartment cell, a urea removal of 86% was obtained after 2.4 h in the anolyte compartment (Fig. 10), with a rate constant of 1.34×10^{-2} min^{-1}. This slight reduction compared to the 90% (1.47×10^{-2} min^{-1}) obtained with the one-compartment cell is attributed to the reduced photoanode potential. Simultaneously, the production of H_2 gas was studied at the catholyte compartment. Hydrogen production reached 3.09×10^{-1} mmol after 1 h irradiation and was confirmed by GC-TCD. This would result in an average 309 μmol h^{-1} rate if a zero order H_2 production rate is assumed. This corresponds to a faradaic efficiency of 87.3%, calculated considering the theoretical mol produced by the recorded current during this hour, 3.54×10^{-1} mmol (Equation S2).

The solar-to-hydrogen conversion efficiency (STH) was calculated by comparing the energy content of the produced hydrogen with the energy supplied by the simulated solar light source (Fig. S1). Using 237 KJ for the energy content of 1 mol of hydrogen and with photoanode area of 19.6 cm^2, an efficiency of 1.1% was obtained (Equation S3). Even the calculated value might seem low, it is important to consider that the maximum theoretical STH for WO_3 is just 4.5% (Li et al., 2013). Raptis et al. (2017) reported STH efficiency varying from 1.2 to 1.7% using WO_3 in presence of ethanol. It is also important to consider that the presence of ethanol is unlikely to be a main component in wastewater and its use as a model pollutant influences the STH because of its known current-doubling effect. Recently, studies have reported the generation of hydrogen and urea oxidation using photoelectrochemistry (Bezboruah et al., 2023; Tao et al., 2022, 2023). Bezboruah et al. (2023) reported the production of H_2 when urea is present in the electrolyte. This study used a Ni–TiO_2/p-NDIHBT photoanode and a Pt cathode in a one compartment cell, achieving a faradaic efficiency of 83.3% and STH efficiency of 0.34%, when using a 0.5 M KOH electrolyte. Tao et al. (2022) demonstrated the oxidation of urea linked to the production of H_2. The study achieved a H_2 production rate of 128 μmol cm^{-2} h^{-1} when employing a La–Ni-based perovskite photoanode and a Pt cathode in a H-cell reactor with 1 M KOH. In a recent study, Tao et al. (2023) studied

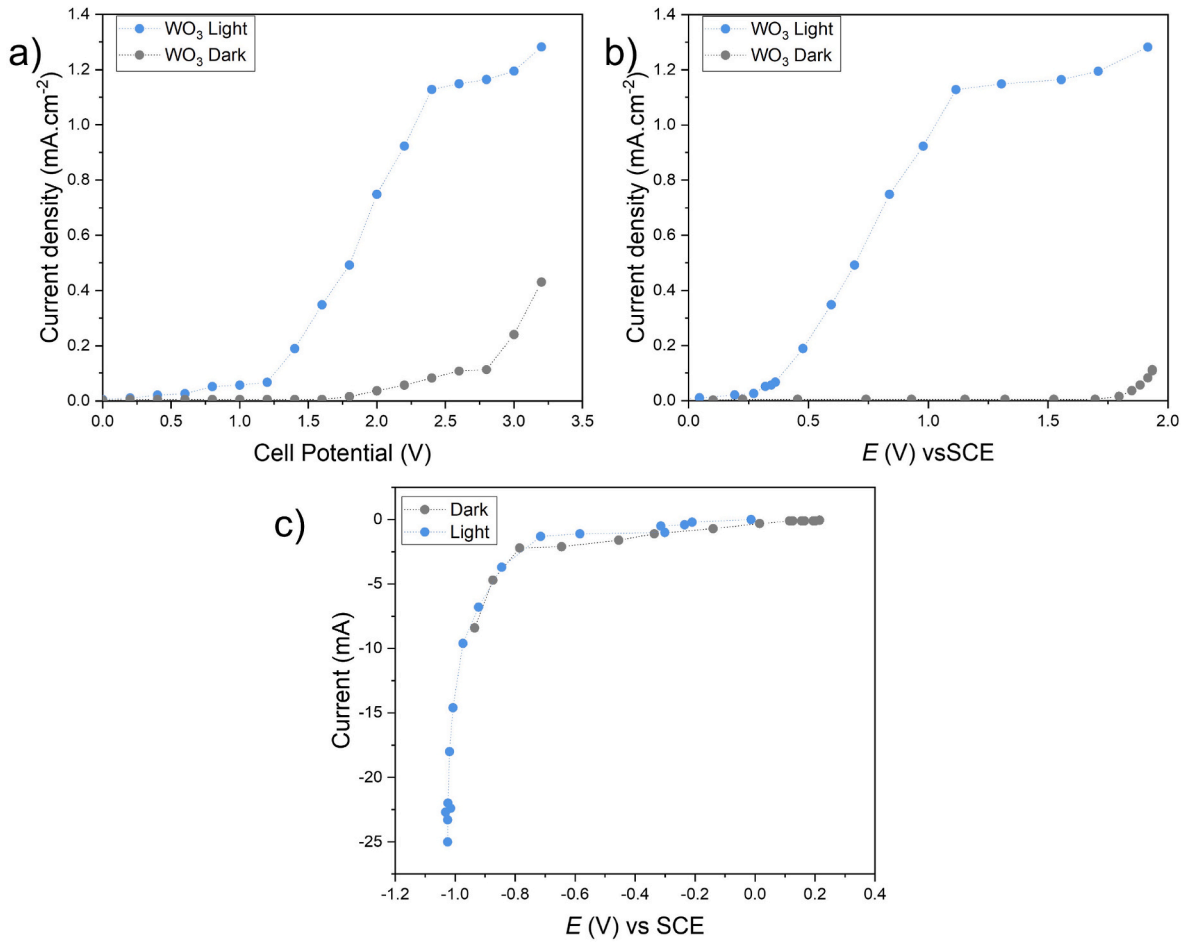

Fig. 9. a) Current vs cell potential for WO_3, b) current vs anode potential for different applied cell potentials c) current vs cathode potential while cell potential is varied. Two-compartment photoelectrochemical cell. I_0 (280–500 nm) = 173 W m^{-2}. Anode geometrical area = 19.6 cm^{-2}. Catholyte electrolyte = 50 mM $KClO_4$ and anolyte electrolyte = 0.83 mM Urea and 50 mM $KClO_4$.

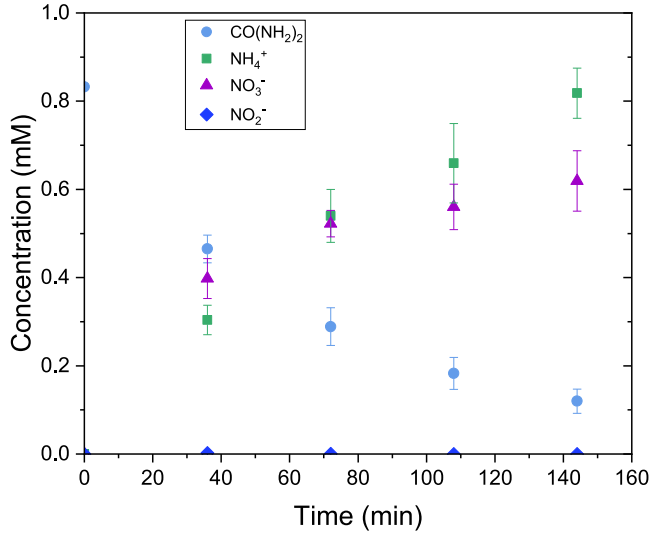

Fig. 10. Degradation of urea and corresponding conversion to NH_4^+, NO_3^- and NO_2^- using WO_3 photoanode. Two-compartment cell. $[Urea]_0$ = 0.83 mM. Electrolyte = 0.05 M $KClO_4$. I_0 (280–500 nm) = 173 W m^{-2}.

the oxidation of urea and hydrogen production, reporting H_2 rate of 200 μmol h^{-1} when using Ni_2P clusters sensitized TiO_2 nanotube arrays photoanode (Ni_2P/TiO_2-NTAs) in a 1 M KOH electrolyte. However, a direct comparison of the performance with the present is not possible due to different experimental testing conditions (as irradiation source, cell configuration and electrolyte). In addition, these studies were performed at alkaline pH (13–14), which if used for wastewater treatment, this process would require pH adjustment of the wastewater with consumable chemicals before treatment and correction before discharge.

In the present study, both the anolyte and catholyte compartment were periodically sampled to identify possible membrane crossover of species. Similar to the observations drawn from the one-compartment cell experiments, the molar nitrogen balance was closed by the summation of the products in solution from both compartments. The products were mostly NH_4^+ and NO_3^-, with a small amount of NO_2^- (Fig. S13d). Small amounts of NH_4^+ are detected in the catholyte compartment, suggesting some NH_4^+ crossover through the membrane. In the case of the two-compartment cell, the measured ratio of NO_3^-/NH_4^+ is equal to 0.76, in close agreement with the 0.81 observed in the one compartment cell.

The NO_2^- concentrations remained below 0.002 mM for the first half of the experiment (Fig. S13), before decreasing below instrumental detection limit (LOD_{NO2} = 2 × 10^{-4} mM). To verify if the observed conversion of NO_3^- to NH_4^+ in the one-compartment cell occurs at the cathode, additional experiments were carried out starting with an initial NO_3^- concentration of 0.55 mM in the anolyte compartment. The

concentration of NO_3^- remains unchanged throughout the duration of the experiments and no detectable concentration of NH_4^+ is found, indicating that the cathode is responsible for the conversion of NO_3^- to NH_4^+ in the one-compartment cell experiments. Additionally, experiments with an initial concentration of 0.58 mM NH_4^+ were performed, similarly to the one-compartment cell no NH_4^+ removal was observed (Fig. S13).

This study has shown the potential of simultaneous photoelectrochemical urea oxidation and hydrogen generation from wastewater. In order to progress from the laboratory scale testing, further work in reactor design is needed. Specifically, a scale-up version of this technology needs to be evaluated in further studies, together with testing with real wastewater, to assess electrode fouling and long-term operation at these conditions. In addition, techno-economic assessment should be carried out before deployment.

4. Conclusions

This work demonstrates the feasibility of coupling urea oxidation to energy recovery as hydrogen. This investigation focuses on the utilization of WO_3 monoclinic plates as photoanode. This visible light active electrode outperformed the UV active TiO_2 electrode for the oxidation of urea without the addition of external oxidizing radicals. WO_3 proved superior urea removal with a rate constant 15 times higher the one obtained for TiO_2.

The coupling of urea oxidation to hydrogen production, besides providing additional value to each individual process, can represent a more desirable anodic process than water splitting to produce hydrogen. This was demonstrated by the increase in photocurrent and IPCE in the presence of urea.

The investigation of the mechanisms of the N-species reactions and product distribution in liquid and gas phase, showed a closed nitrogen balance with nitrate and ammonium as main by-products and the production of hydrogen with a faradaic efficiency of 87.3% and a STH efficiency of 1.1%. Nitrite was just detected in small quantities as it rapidly converted to nitrate. Moreover, the use of a two-compartment PEC should be considered to separate gas products and to limit the side reactions at the cathode derived by anode by-products. Further work is needed to address the preferential and selective oxidation of urea to dinitrogen.

This study showcases the potential of photoelectrochemical urea oxidation and hydrogen generation from wastewater. This technology can achieve the recovery of resources from wastewater, generating a clean fuel, which aids in the implementation of the circular economy concept and the development of sustainable approaches in the environmental and energy fields. The presented findings encourage further developments related to coupling of wastewater remediation to energy recovery.

CRediT authorship contribution statement

Adriana Rioja-Cabanillas: Conceptualization, Methodology, Investigation, Writing – original draft, Writing – review & editing. **Stuart McMichael:** Investigation, Writing – review & editing. **Alvaro Tolosana-Moranchel:** Writing – review & editing. **Salem Alkharabsheh:** Writing – review & editing. **Nathan Skillen:** Investigation, Writing – review & editing. **Pilar Fernandez-Ibanez:** Writing – review & editing, Supervision, Funding acquisition. **John Anthony Byrne:** Writing – review & editing, Supervision, Funding acquisition.

Declaration of competing interest

The authors declare that they have no known competing financial interests or personal relationships that could have appeared to influence the work reported in this paper.

Data availability

Data will be made available on request.

Acknowledgements

This work was supported by the European Union's Horizon 2020 research and innovation programme under the Marie-Curie grant agreement No 812574 (REWATERGY) and under grant agreement No 820718 (PANIWATER). Álvaro Tolosana Moranchel also thanks the Consejería de Educación, Juventud y Deporte of the Comunidad de Madrid for the Ayuda Destinada a la Atracción de Talento Investigador (2020-T2/AMB-19927) granted to him. The authors also thank Delft-IMP for supporting this research.

Appendix A. Supplementary data

Supplementary data to this article can be found online at https://doi.org/10.1016/j.jclepro.2023.138200.

References

Alov, N.V., 2005. Determination of the states of oxidation of metals in thin oxide films by X-ray photoelectron spectroscopy. J. Anal. Chem. 60, 431–435. https://doi.org/10.1007/s10809-005-0114-x.

Bezboruah, J., Sanke, D.M., Munde, A.V., Das, S., Karmakar, H.S., Zade, S.S., 2023. Nickel-doped TiO2 and thiophene-naphthalenediimide copolymer based inorganic/organic nano-heterostructure for the enhanced photoelectrochemical urea oxidation reaction. Int. J. Hydrogen Energy 48, 7361–7373. https://doi.org/10.1016/j.ijhydene.2022.11.098.

Bharti, B., Kumar, S., Lee, H.N., Kumar, R., 2016. Formation of oxygen vacancies and Ti3 + state in TiO2 thin film and enhanced optical properties by air plasma treatment. Sci. Rep. 6, 1–12. https://doi.org/10.1038/srep32355.

Boggs, B.K., King, R.L., Botte, G.G., 2009. Urea electrolysis: direct hydrogen production from urine. Chem. Commun. 4859–4861. https://doi.org/10.1039/b905974a.

BP Statistical Review of World Energy, 2021. BP [WWW Document]. URL. https://www.bp.com/content/dam/bp/business-sites/en/global/corporate/pdfs/energy-economics/statistical-review/bp-stats-review-2022-full-report.pdf. (Accessed 12 May 2022).

Calza, P., Pelizzetti, E., Minero, C., 2005. The fate of organic nitrogen in photocatalysis: an overview. J. Appl. Electrochem. 35, 665–673. https://doi.org/10.1007/s10800-005-1626-7.

Corby, S., Francàs, L., Kafizas, A., Durrant, J.R., 2020. Determining the role of oxygen vacancies in the photoelectrocatalytic performance of WO3 for water oxidation. Chem. Sci. 11, 2907–2914. https://doi.org/10.1039/c9sc06325k.

Dector, D., Ortega-Díaz, D., Olivares-Ramírez, J.M., Dector, A., Pérez-Bueno, J.J., Fernández, D., Amaya-Cruz, D.M., Reyes-Rojas, A., 2021. Harvesting energy from real human urine in a photo-microfluidic fuel cell using TiO2–Ni anode electrode. Int. J. Hydrogen Energy 46, 26163–26173. https://doi.org/10.1016/j.ijhydene.2021.02.148.

Dutta, V., Sharma, S., Raizada, P., Kumar, V., 2021. An overview on WO3 based photocatalyst for environmental remediation. J. Environ. Chem. Eng. 9, 105018 https://doi.org/10.1016/j.jece.2020.105018.

Egle, L., Rechberger, H., Zessner, M., 2015. Resources , Conservation and Recycling Overview and description of technologies for recovering phosphorus from municipal wastewater. Resour. Conserv. Recycl. 105, 325–346. https://doi.org/10.1016/j.resconrec.2015.09.016.

Fernandez-Ibanez, P., McMichael, S., Rioja Cabanillas, A., Alkharabsheh, S., Tolosana Moranchel, A., Byrne, J.A., 2021. New trends on photoelectrocatalysis (PEC): nanomaterials, wastewater treatment and hydrogen generation. Curr. Opin. Chem. Eng. 34, 100725 https://doi.org/10.1016/j.coche.2021.100725.

Greiner, M.T., Chai, L., Helander, M.G., Tang, W.-M., Lu, Z.-H., 2012. Transition metal oxide work functions: the influence of cation oxidation state and oxygen vacancies. Adv. Funct. Mater. 22, 4557–4568. https://doi.org/10.1002/adfm.201200615.

Haisch, C., Schneider, J., Fleisch, M., Gutzmann, H., Klassen, T., Bahnemann, D.W., 2017. Cold sprayed WO3 and TiO2 electrodes for photoelectrochemical water and methanol oxidation in renewable energy applications. Dalton Trans. 46, 12811–12823. https://doi.org/10.1039/c7dt02063e.

IRENA, 2021. Green Hydrogen Supply: A Guide to Policy Making [WWW Document]. URL. https://www.irena.org/-/media/Files/IRENA/Agency/Publication/2021/May/IRENA_Green_Hydrogen_Supply_2021.pdf. (Accessed 12 October 2022).

Jung, D., Biggs, H., Erikson, J., Ledyard, P.U., 1975. New colorimetric reaction for end point, continuous flow, and kinetic measurement of urea. Clin. Chem. 21, 1136–1140. https://doi.org/10.1093/clinchem/21.8.1136.

Kalanur, S.S., Duy, L.T., Seo, H., 2018. Recent progress in photoelectrochemical water splitting activity of WO3 photoanodes. Top. Catal. 61, 1043–1076. https://doi.org/10.1007/s11244-018-0950-1.

Kaneko, M., Nemoto, J., Ueno, H., Gokan, N., Ohnuki, K., Horikawa, M., Saito, R., Shibata, T., 2006. Photoelectrochemical reaction of biomass and bio-related

compounds with nanoporous TiO2 film photoanode and O2-reducing cathode. Electrochem. Commun. 8, 336–340. https://doi.org/10.1016/j.elecom.2005.12.004.
Kim, J., Monllor-Satoca, D., Choi, W., 2012. Simultaneous production of hydrogen with the degradation of organic pollutants using TiO2 photocatalyst modified with dual surface components. Energy Environ. Sci. 5, 7647–7656. https://doi.org/10.1039/c2ee21310a.
Kim, K., Kim, M.J., Kim, S.I., Jang, J.-H., 2013. Towards visible light hydrogen generation: quantum dot-sensitization via efficient light harvesting of hybrid-TiO2. Sci. Rep. 3, 1–8. https://doi.org/10.1038/srep03330.
Lens, P., Hulshoff Pol, L., Wilderer, P., Asano, T., 2005. Water Recycling and Resource Recovery in Industry: Analysis, Technologies and Implementation. IWA Publishing. https://doi.org/10.2166/9781780402802.
Li, W., Da, P., Zhang, Y., Wang, Y., Lin, X., Gong, X., Gengfeng, Z., 2014. WO3 nanoflakes for enhanced photoelectrochemical conversion. ACS Nano 8, 11770–11777.
Li, Y., Wei, X., Yan, X., Cai, J., Zhou, A., Yang, M., Liu, K., 2016. Construction of inorganic-organic 2D/2D WO3/g-C3N4 nanosheet arrays toward efficient photoelectrochemical splitting of natural seawater. Phys. Chem. Chem. Phys. 18, 10255–10261. https://doi.org/10.1039/c6cp00353b.
Li, Z., Luo, W., Zhang, M., Feng, J., Zou, Z., 2013. Photoelectrochemical cells for solar hydrogen production: current state of promising photoelectrodes, methods to improve their properties, and outlook. Energy Environ. Sci. 6, 347–370. https://doi.org/10.1039/c2ee22618a.
Liu, J., Xu, S.M., Li, Y., Zhang, R., Shao, M., 2020. Facet engineering of WO3 arrays toward highly efficient and stable photoelectrochemical hydrogen generation from natural seawater. Appl. Catal. B Environ. 264, 118540 https://doi.org/10.1016/j.apcatb.2019.118540.
Liu, X., Wang, F., Wang, Q., 2012. Nanostructure-based WO 3 photoanodes for photoelectrochemical water splitting. Phys. Chem. Chem. Phys. 14, 7894–7911. https://doi.org/10.1039/c2cp40976c.
Liu, Y., Chang, Y.S., Hsu, Y.J., Hwang, B.J., Hsueh, C.H., 2019. Fabrication of WO3 photoanode decorated with Au nanoplates and its enhanced photoelectrochemical properties. Electrochim. Acta 321, 134674. https://doi.org/10.1016/j.electacta.2019.134674.
McMurray, T.A., Byrne, J.A., Dunlop, P.S.M., Winkelman, J.G.M., Eggins, B.R., McAdams, E.T., 2004. Intrinsic kinetics of photocatalytic oxidation of formic and oxalic acid on immobilised TiO2 films. Appl. Catal. Gen. 262, 105–110. https://doi.org/10.1016/j.apcata.2003.11.013.
McMurray, T.A., Dunlop, P.S.M., Byrne, J.A., 2006. The photocatalytic degradation of atrazine on nanoparticulate TiO2 films. J. Photochem. Photobiol. Chem. 182, 43–51. https://doi.org/10.1016/j.jphotochem.2006.01.010.
Michels, N.L., Kapałka, A., Abd-El-Latif, A.A., Baltruschat, H., Comninellis, C., 2010. Enhanced ammonia oxidation on BDD induced by inhibition of oxygen evolution reaction. Electrochem. Commun. 12, 1199–1202. https://doi.org/10.1016/j.elecom.2010.06.018.
Nemoto, J., Gokan, N., Ueno, H., Kaneko, M., 2007. Photodecomposition of ammonia to dinitrogen and dihydrogen on platinized TiO2 nanoparticles in an aqueous solution. J. Photochem. Photobiol. Chem. 185, 295–300. https://doi.org/10.1016/j.jphotochem.2006.06.024.
Park, S., Lee, J.T., Kim, J., 2019. Photocatalytic oxidation of urea on TiO2 in water and urine: mechanism, product distribution, and effect of surface platinization. Environ. Sci. Pollut. Res. 26, 1044–1053. https://doi.org/10.1007/s11356-017-8380-3.
Pelaez, M., Nolan, N.T., Pillai, S.C., Seery, M.K., Falaras, P., Kontos, A.G., Dunlop, P.S.M., Hamilton, J.W.J., Byrne, J.A., O'Shea, K., Entezari, M.H., Dionysiou, D.D., 2012. A review on the visible light active titanium dioxide photocatalysts for environmental applications. Appl. Catal. B Environ. 125, 331–349. https://doi.org/10.1016/j.apcatb.2012.05.036.
Pelizzetti, E., Calza, P., Mariella, G., Maurino, V., Minero, C., Hidaka, H., 2004. Different photocatalytic fate of amido nitrogen in formamide and urea. Chem. Commun. 4, 1504–1505. https://doi.org/10.1039/b404574b.
Pop, L.C., Tantis, I., Lianos, P., 2015. Photoelectrocatalytic hydrogen production using nitrogen containing water soluble wastes. Int. J. Hydrogen Energy 40, 8304–8310. https://doi.org/10.1016/j.ijhydene.2015.04.116.
Ranganathan, K., Morais, A., Nongwe, I., Longo, C., Nogueira, A.F., Coville, N.J., 2016. Study of photoelectrochemical water splitting using composite films based on TiO2 nanoparticles and nitrogen or boron doped hollow carbon spheres as photoanodes. J. Mol. Catal. Chem. 422, 165–174. https://doi.org/10.1016/j.molcata.2015.10.024.
Raptis, D., Dracopoulos, V., Lianos, P., 2017. Renewable energy production by photoelectrochemical oxidation of organic wastes using WO3 photoanodes. J. Hazard Mater. 333, 259–264. https://doi.org/10.1016/j.jhazmat.2017.03.044.
Reddy, C.V., Reddy, K.R., Shetti, N.P., Shim, J., Aminabhavi, T.M., Dionysiou, D.D., 2020. Hetero-nanostructured metal oxide-based hybrid photocatalysts for enhanced photoelectrochemical water splitting – a review. Int. J. Hydrogen Energy 45, 18331–18347. https://doi.org/10.1016/j.ijhydene.2019.02.109.
Rioja-Cabanillas, A., Valdesueiro, D., Fernández-Ibáñez, P., Byrne, J.A., 2020. Hydrogen from wastewater by photocatalytic and photoelectrochemical treatment. J. Phys. Energy 3, 12006. https://doi.org/10.1088/2515-7655/abceab.
Rollinson, A.N., Jones, J., Dupont, V., Twigg, M.V., 2011. Urea as a hydrogen carrier: a perspective on its potential for safe, sustainable and long-term energy supply. Energy Environ. Sci. 4, 1216–1224. https://doi.org/10.1039/C0EE00705F.
Shen, Z., Bai, J., Zhang, Y., Li, J., Zhou, T., Wang, J., Xu, Q., Zhou, B., 2019a. Efficient purification and chemical energy recovery from urine by using a denitrifying fuel cell. Water Res. 152, 117–125. https://doi.org/10.1016/j.watres.2018.12.066.
Shen, Z., Li, J., Zhang, Y., Bai, J., Tan, X., Li, X., Qiao, L., Xu, Q., Zhou, B., 2019b. Highly efficient total nitrogen and simultaneous total organic carbon removal for urine based on the photoelectrochemical cycle reaction of chlorine and hydroxyl radicals. Electrochim. Acta 297. https://doi.org/10.1016/j.electacta.2018.11.087.
Shen, Z., Zhang, Y., Zhou, C., Bai, J., Chen, S., Li, J., Wang, J., Guan, X., Rahim, M., Zhou, B., 2020. Exhaustive denitrification via chlorine oxide radical reactions for urea based on a novel photoelectrochemical cell. Water Res. 170, 115357 https://doi.org/10.1016/j.watres.2019.115357.
Tao, Y., Chen, L., Ma, Z., Zhang, C., Zhang, Y., Zhang, D., Pan, D., Wu, J., Li, G., 2022. Near-infrared-driven photoelectrocatalytic oxidation of urea on La-Ni-based perovskites. Chem. Eng. J. 446, 137240 https://doi.org/10.1016/j.cej.2022.137240.
Tao, Y., Ma, Z., Wang, W., Zhang, C., Fu, L., Zhu, Q., Li, Y., Li, G., Zhang, D., 2023. Nickel phosphide clusters sensitized TiO2 nanotube arrays as highly efficient photoanode for photoelectrocatalytic urea oxidation. Adv. Funct. Mater. 33, 2211169 https://doi.org/10.1002/adfm.202211169.
Tolosana-Moranchel, A., Pichel, N., Lubarsky, H., Byrne, J.A., Fernández-Ibañez, P., 2022. Photoelectrocatalytic degradation of pharmaceuticals and inactivation of viruses in water with tungsten oxide electrodes. J. Environ. Chem. Eng. 10, 107955 https://doi.org/10.1016/j.jece.2022.107955.
Wang, G., Ling, Y., Lu, X., Wang, H., Qian, F., Tong, Y., Li, Y., 2012. Solar driven hydrogen releasing from urea and human urine. Energy Environ. Sci. 5, 8215–8219. https://doi.org/10.1039/c2ee22087c.
Wang, Y., Zu, M., Zhou, X., Lin, H., Peng, F., Zhang, S., 2020. Designing efficient TiO2-based photoelectrocatalysis systems for chemical engineering and sensing. Chem. Eng. J. 381, 122605 https://doi.org/10.1016/j.cej.2019.122605.
Water quality — Determination of Selected Parameters by Discrete Analysis Systems BS ISO 15923-1:2013, 2013.
Yang, J., Li, W., Li, J., Sun, D., Chen, Q., 2012. Hydrothermal synthesis and photoelectrochemical properties of vertically aligned tungsten trioxide (hydrate) plate-like arrays fabricated directly on FTO substrates. J. Mater. Chem. 22, 17744–17752. https://doi.org/10.1039/C2JM33199C.
Yang, Z., Jiang, Yunhong, Zhang, W., Ding, Y., Jiang, Yong, Yin, J., Zhang, P., Luo, H., 2019. Solid-state, low-cost, and green synthesis and robust photochemical hydrogen evolution performance of ternary TiO2/mgTiO3/C photocatalysts. iScience 14, 15–26. https://doi.org/10.1016/j.isci.2019.03.009.
Yu, H., Zhao, Y., Zhou, C., Shang, L., Peng, Y., Cao, Y., Wu, L.Z., Tung, C.H., Zhang, T., 2014. Carbon quantum dots/TiO2 composites for efficient photocatalytic hydrogen evolution. J. Mater. Chem. 2, 3344–3351. https://doi.org/10.1039/c3ta14108j.
Zafra, A., Garcia, J., Milis, A., Domènech, X., 1991. Kinetics of the catalytic oxidation of nitrite over illuminated aqueous suspensions of TiO2. J. Mol. Catal. 70, 343–349. https://doi.org/10.1016/0304-5102(91)80129-Q.
Zawada, R.J.X., Kwan, P., Olszewski, K.L., Llinas, M., Huang, S.G., 2009. Quantitative determination of urea concentrations in cell culture medium. Biochem. Cell. Biol. 87, 541–544. https://doi.org/10.1139/O09-011.
Zeng, Q., Li, J., Bai, J., Li, X., Xia, L., Zhou, B., 2017. Preparation of vertically aligned WO3 nanoplate array films based on peroxotungstate reduction reaction and their excellent photoelectrocatalytic performance. Appl. Catal. B Environ. 202, 388–396. https://doi.org/10.1016/j.apcatb.2016.09.045.
Zheng, G., Wang, J., Liu, H., Murugadoss, V., Zu, G., Che, H., Lai, C., Li, H., Ding, T., Qiang, G., Guo, Zhanhu, 2019. Tungsten oxide nanostructures and nanocomposites for photoelectrochemical water splitting. Nanoscale, 18968. https://doi.org/10.1039/c9nr03474a, 18968–18994.
Zhu, X., Castleberry, S.R., Nanny, M.A., Butler, E.C., 2005. Effects of pH and catalyst concentration on photocatalytic oxidation of aqueous ammonia and nitrite in titanium dioxide suspensions. Environ. Sci. Technol. 39, 3784–3791. https://doi.org/10.1021/es0485715.